PHOTONICS Research

Quantum positioning and ranging via a distributed sensor network

Xiaocong Sun,[1,†] Wei Li,[1,2,†] Yuhang Tian,[1] Fan Li,[1] Long Tian,[1,2] Yajun Wang,[1,2] and Yaohui Zheng[1,2,*]

[1]State Key Laboratory of Quantum Optics and Quantum Optics Devices, Institute of Opto-Electronics, Shanxi University, Taiyuan 030006, China
[2]Collaborative Innovation Center of Extreme Optics, Shanxi University, Taiyuan 030006, China
*Corresponding author: yhzheng@sxu.edu.cn

Received 29 June 2022; revised 8 October 2022; accepted 26 October 2022; posted 27 October 2022 (Doc. ID 469166); published 1 December 2022

A quantum sensor network with multipartite entanglement offers a sensitivity advantage in optical phase estimation over the classical scheme. To tackle richer sensing problems, we construct a distributed sensor network with four nodes via four partite entanglements, unveil the estimation of the higher order derivative of radio-frequency signal phase, and unlock the potential of quantum target ranging and space positioning. Taking phased-array radar as an example, we demonstrate the optimal quantum advantages for space positioning and target ranging missions. Without doubt, the demonstration that endows innovative physical conception opens up widespread application of quantum sensor networks.

https://doi.org/10.1364/PRJ.469166

1. INTRODUCTION

Quantum metrology provides a route to conquer the measurement sensitivity limitation imposed by quantum noise in sensing devices [1–3]. As a unique quantum resource, squeezed and entangled states present the feature of quantum correlation, which can suppress statistical scaling of errors $n^{-\frac{1}{2}}$ in interferometric measurements, and thereby enhance measurement precision, until approaching and reaching the Heisenberg bound $1/n$ [4–6]. It holds particular relevance to the power constraint introduced by optical damage or quantum measurement backaction, and an ultra-weak signal that is thoroughly submerged in inherent quantum noise. Laser radar is a prime case of ultra-weak signal sensing, and has an urgent demand for measurement sensitivity beyond the shot noise limit [7,8].

Since quantum metrology was recognized in the 1980s [9], both the theoretical scheme and experimental technology of quantum metrology have advanced dramatically [10,11]. In this regard, numerous demonstrations of quantum-enhanced metrology have been reported, for example, to enhance the performance of gravitational wave detection [12–15], magnetic field detection [16,17], and biological measurement [18] and imaging [19,20], and are expected to be applied in more practical areas. Furthermore, quantum sensing has been upgraded from a single sensor to a sensor network to realize spatially distributed sensing of multi-parameters. Theoretical schemes of distributed quantum sensing have been proposed in both the discrete variable (DV) domain [21–24] and continuous variable (CV) domain [25–29]. By utilizing entangled photons [30,31] or entangled states [32], the average optical phase was estimated experimentally with precision beyond what is achievable with seperable probes. Very recently, Xia *et al.* extended the application of distributed quantum sensing to a radio-frequency signal based on tripartite CV entanglement [33], and subsquently demonstrated the supervised learning assisted by an entangled sensor network for quantum-enhanced data classification [34]. Taking a typical sensing mission for phased-array radar (PAR) as an example, the fundamental requirement is to be able to discover a target and acquire its position relative to the sensor, not only to discriminate whether the target is present or not. However, for space positioning of a moving target with PAR, it is necessary to estimate three angles of arrival simultaneously, which cannot be implemented by three sensor nodes [33]. Moreover, estimating the angle of arrival and its derivative with high accuracy is necessary to implement target ranging, requiring at least four sensor nodes. In addition, the power limit of laser radar that comes from the endless pursuit of the detecting range is ultimately determined by noise performance. For a classical system, poor noise performance imposes restrictions on the intensity of the return signal, and that in turn limits the detecting range, which has the potential to be improved to some extent via squeezed light. To date, quantum positioning [35,36] and quantum ranging [37] protocols based on multipartite entanglement have been proposed theoretically, but none of these protocols have been demonstrated experimentally.

In this paper, we experimentally demonstrate a quantum sensor network empowered by four-partite CV entanglement, optimizing the quantum advantage in global parameter estimation including the higher order derivative of radio-frequency

signal phase. The global parameter of four sensors $\varphi = \sum_{j=1}^{4} \beta_j \varphi_j$, where β_j is the weights for different sensing problems, is estimated in our experiment, achieving quantum noise reduction of 6.0 dB ± 0.2 dB. The quantum sensor network is configured with an equally weighted distribution to maximize the quantum advantage for measuring the angle of arrival of the return signal along three independent dimensions, showing quantum positioning. The sensor network is reconfigured with a weighted distribution of −11/6:3:−3/2:1/3 (2:−5:4:−1) to maximize the quantum advantage of the first (second) derivative of PAR phase, demonstrating quantum ranging.

PAR consists of multiple sensing elements appropriately arranged in space, whose amplitude and phase can be independently controlled to provide full space scanning without the influence of receiving sensitivity [38]. Space positioning can be realized by measuring the angle of arrival of the return signal in three dimensions [39], which can be inferred from the phase difference between two sensor nodes of each dimension [33]. Thus, to achieve space positioning, it requires at least four sensor nodes. As the other key capacity, target ranging, dependent on the angle of arrival and its derivative of the return signal in one dimension, can be obtained by configuring a diverse weighted distribution among these sensor nodes. As such, a reconfigurable beam splitter network (BSN), in terms of minimum estimation variance, distributes the needed portion of a squeezed state to these sensor nodes, leading to the optimal quantum advantage in different cases, which serves as the estimation of the angle of arrival and its first (second) derivative beyond the shot noise limit. There are two cases of sensor network topology: equilateral star topology for space positioning, and linear topology for target ranging. Compared with the demonstration of only an average outcome among all of sensor nodes, the richer physics and more intriguing application scenario of a distributed quantum sensor network are unveiled by our work.

2. QUANTUM POSITIONING PROTOCOL

In the quantum positioning case, three sensor nodes are arranged in an equilateral star topology, while the central node is situated at the triangle center; the schematic illustration of quantum positioning is represented in Fig. 1. When the target occurs, we can acquire three independent angles of arrival in three-dimensional space, and the target is positioned at the intersectional region of three angles of arrival. Critically, the distributed quantum sensor network must be optimized to generate minimum outcome uncertainty in a given distributed sensing problem. Here, to meet the requirement for simultaneous estimation of three angles of arrival with minimum positioning uncertainty, dependent on the phase difference between two sensor nodes with the function of $\theta = \arccos\frac{\lambda(\varphi_j - \varphi_1)}{2\pi\Delta x}$ $(j = 2, 3, 4)$, a CV quantum sensor network with an equally weighted distribution is constructed. Under the circumstances, the additional noise coupling vanishes, leading to the minimum estimation variance of the PAR phase that depends on the initial squeezing factor. The equally weighted distribution is experimentally verified when the average variance for PAR phase $\varphi = \sum_{j=1}^{4} \beta_j \varphi_j$ ($\beta_4 = \beta_3 = \beta_2 = 1$, $\beta_1 = -1$) reaches minimum. At this point, the uncertainties of three phase differences $\varphi_2 - \varphi_1$, $\varphi_3 - \varphi_1$, and $\varphi_4 - \varphi_1$ represent the best compromise, and will have a boosted performance for target positioning.

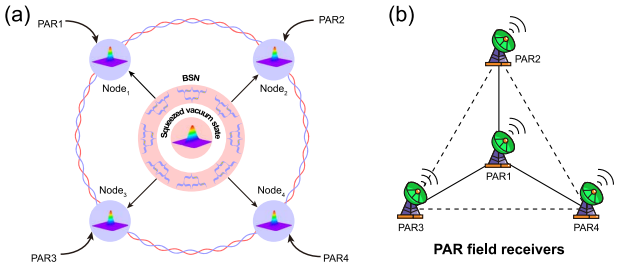

Fig. 1. Schematic illustration of quantum positioning based on CV entangled network. (a) Principle of quantum positioning. (b) Structural diagram of PAR network.

A schematic illustration of our experimental setup is represented in Fig. 2. The squeezed state of light is generated by a below-threshold optical parametric amplifier (OPA), which has been shown in our previous publication in details [40]. The only difference is that the relative phase between the seed and pump beam is controlled to zero to ensure our OPA operates in parametric amplification condition, generating the quadrature phase squeezed state [$\delta^2(\hat{Y}) = e^{-2r}$; r is the squeezing factor]. The BSN, which consists of three pairs of half-wave plates and polarization beam splitters, can be set to any splitting ratio by tuning the angle of half-wave plates. After the BSN, four partite CV entangled states with correlation variance [$\delta^2(\beta_1\hat{Y}_1 + \beta_2\hat{Y}_2 + \beta_3\hat{Y}_3 + \beta_4\hat{Y}_4) = e^{-2r}$; $\hat{Y}_i$ $(i = 1, 2, 3, 4)$ is the phase quadrature of each partite] are generated and distributed to four sensor nodes. Each sensor node entails an electro-optical modulator (EOM) to simulate the return signal from the target, and homodyne detection (HOM) to discern the return signal with sensitivity beyond the shot noise limit. In each node, the relative phase between the local oscillator and sensing beam is controlled to $\pm\pi/2$ by utilizing the interference signal as the error signal. The EOM that has high radio frequency to photonics conversion efficiency, is an excellent simulator of PAR. Four EOMs are independently driven by four clock-synchronized function generators with the same modulation frequency of 3 MHz, but the amplitude and phase are independently manipulated to generate four independent displacements α_j $(j = 1, 2, 3, 4)$ on the squeezed phase quadrature [33]. The output of four homodyne detectors through the same four bandpass filters from 1.8 MHz to 4.5 MHz is demodulated with 3 MHz signals. The demodulation signals are clock synchronized with the corresponding return signals, but their phases can be independently manipulated to compensate for the delay difference of the processing circuit. The time-domain data from four mixers are collected and postprocessed to derive the estimated parameters under different weights, and demonstrate diverse quantum-enhanced sensing applications.

The noise variances of the measured PAR phase are limited by the initial squeezing factor and system loss. It is worth noting that the parametric amplification process (for the generation of a quadrature phase squeezed state) intensifies the noise coupling between the seed and pump field, which usually results in the degradation of the squeezing factor [41]. As the

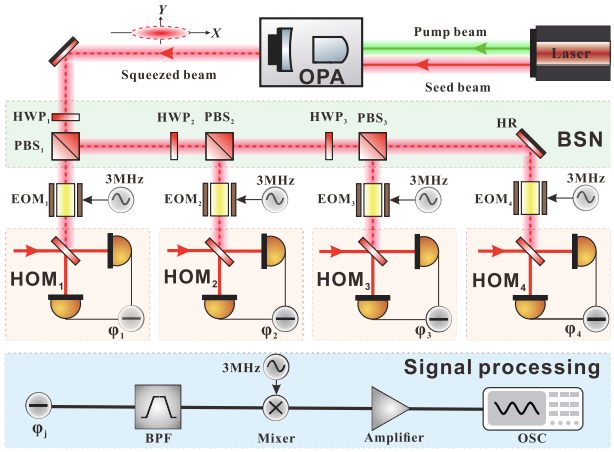

Fig. 2. Experimental setup of quantum-enhanced PAR with a CV entangled network. OPA, optical parametric amplifier; HWP, half-wave plate; PBS, polarization beam splitter; BSN, beam splitter network; EOM, electro-optical modulator; HOM, homodyne detection. BPF, bandpass filter.

pump factor is increased, the noise coupling is enhanced. Thus, we need to make a trade-off between the pump factor and noise coupling, both of which are key factors affecting the squeezing factor. Here, the OPA operates at the pump factor of $\sqrt{2}/2$, with quantum noise reduction of 8.0 ± 0.2 dB generated, providing a superior quantum resource for the downstream experiment.

During the experiment, delicate mode-matching with interference efficiency of 99.8% is accomplished. The optimal weights are scheduled in terms of the different mission requirements, and the number of optical elements is as small as possible, reducing the additional noise coupling to the maximum extent and minimizing the estimation variance of diverse physical scenarios. On the other hand, the phase of the demodulation signal is carefully optimized to suppress the noise coupling of anti-squeezing quadrature into squeezing quadrature as much as possible.

Suppose that the PAR operates in single-transmitter and multi-receiver mode; we show the experimental results of quantum-enhanced PAR in two sensing tasks. PAR1 serves as a transmitter and receiver, and all other nodes act as receivers.

Under ideal conditions, three angles of arrival define a point in space, which is the principle of target positioning. More details can be found in Appendix A. However, the quantum noise of an optical field imposes a limitation on positioning precision, defining a space region instead of a point. Positioning precision can be improved by reducing the estimation variance of each angle of arrival. According to the above analysis, a quantum sensor network with an equally weighted distribution can offer a precision advantage in the angle of arrival estimation over the other weighted one. We estimate the average displacement for radio-frequency phase ($\varphi = \varphi_4 + \varphi_3 + \varphi_2 - \varphi_1$) by measuring the phase quadrature of each node and summing the photocurrents of four homodyne detectors. Figure 3(a) represents the estimation of average field amplitude and estimation variance for φ as a function of the applied PAR phases for all

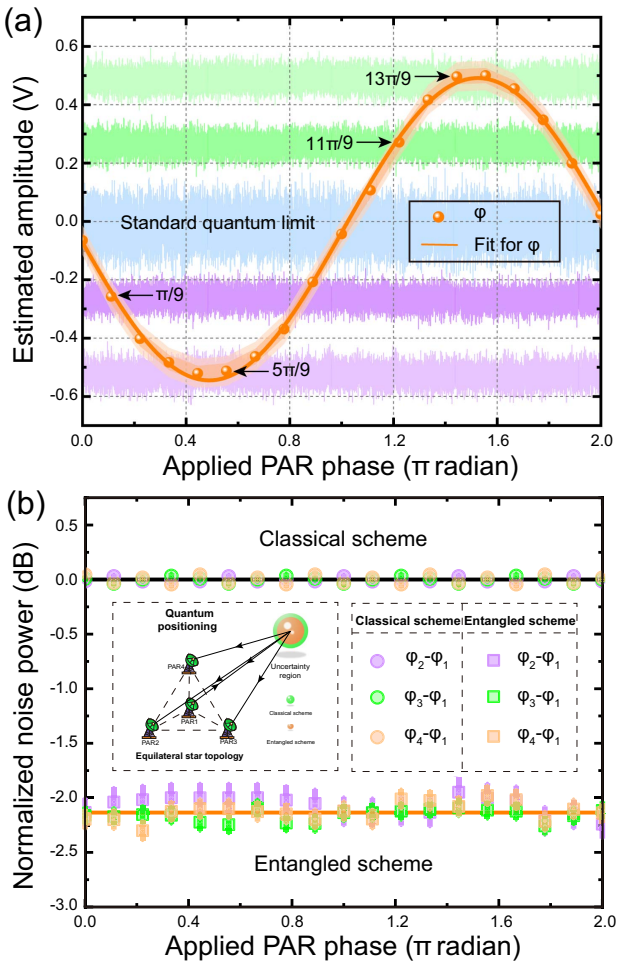

Fig. 3. Estimation of average field amplitude and normalized noise powers versus applied PAR phases. (a) Estimated average field amplitude. Data points: average displacement from homodyne detection; orange curves: sinusoidal fit; orange shaded area: estimation uncertainties for the entangled (dark color) and classical separable (light color) sensor networks. The blue curve shows the time-domain measurement result of standard quantum limit; the purple, light purple, green, and light green curves represent the measurement results with the entangled sensor network at several PAR phases: $\pi/9$, $5\pi/9$, $11\pi/9$, and $13\pi/9$, respectively. (b) Measured noise powers of three phase differences. Black and orange curves show the noise powers based on classical and entangled schemes, respectively. The circular and square data points represent noise powers of three different phase differences with classical and entangled schemes, respectively. All measurement results are normalized to the standard quantum limit.

sensors synchronously. We repeatedly measured the dependence of estimated amplitude (average displacement) on applied PAR phase from zero to 2π with phase interval of 20 deg. To reach optimum estimation precision, the applied PAR phase is manipulated to generate identical displacements on the phase quadrature in each sensor node simultaneously. By minimizing the estimation variance, a 6.0 dB $\pm$ 0.2 dB quantum noise reduction is achieved, confirming the entanglement properties of the sensor network with equally weighted distribution. At this point, the splitting ratios of three variable beam splitters (VBSs) are 25:75, 33:67, and 50:50, and the three angles of

arrival are quantified. Figure 3(b) shows the measured noise powers for three phase differences $\varphi_j - \varphi_1$ $(j = 2, 3, 4)$ for estimating the angle of arrival at different applied PAR phases. The measurement noise variances of three phase differences, represented by purple, green, and orange, are plotted for both quantum (square) and classical (circle) cases. The estimation variances for several cases are normalized to the shot noise limit. It is evident that the quantum-enhanced sensor network leads to a reduction in estimation variance, whereas such a noise reduction mechanism is absent without the quantum resource. The reduced noise powers of -2.1 ± 0.1 dB for $\varphi_2 - \varphi_1$, -2.2 ± 0.1 dB for $\varphi_3 - \varphi_1$, and -2.1 ± 0.1 dB for $\varphi_4 - \varphi_1$ are obtained, which means the detection range is expanded by at least 12.8%. The noise variances are independent of the applied PAR phases, allowing the realization of 360-deg arbitrary scanning. The inset of Fig. 3(b) shows the principle of the improved positioning precision. It can be inferred that the uncertainty region of our protocol with multipartite entanglement is reduced to 0.4837 in three-dimensional space, in contrast with the classical protocol, corresponding to positioning precision improvement of 51.6%. Suppose we individually estimate each phase difference $\varphi_2 - \varphi_1$ ($\varphi_3 - \varphi_1$, $\varphi_4 - \varphi_1$) with the optimal weights 1/2:1/2:0:0 (1/2:0:1/2:0, 1/2:0:0:1/2); then we can obtain higher sensitivity improvement (6.8 dB) than that of simultaneous estimation using similar quantum states. However, the individual estimation will spend more time performing the measurement task (three times), which is inappropriate for the positioning protocol of a moving target.

3. QUANTUM RANGING PROTOCOL

In the quantum ranging case, except for target positioning, target ranging is another critical specification of a radar system, which can be expressed as (see Appendix B for more details)

$$r = \frac{(\varphi_1')^2}{\varphi_1''} \frac{\lambda}{36\pi\Delta x}(-\sin\zeta x' - \cos\zeta y' + iz'), \tag{1}$$

where φ_1' and φ_1'' are the first and second derivatives of edge node PAR1; λ is the wavelength of the PAR field; Δx indicates the distance between each two sensors; x', y', and z' show the movement speed of a target; ζ represents the azimuth angle of a target in terms of the PAR plane. The azimuth angle ζ can be obtained from the positioning case demonstrated in the previous section. According to Eq. (1), target ranging can be transferred to the estimation of the first and second derivatives of edge node PAR1. Exploiting the Taylor series expansion of the phase estimator with the estimated phase φ_1 of edge node PAR1 [33], the optimum weights for the first and second derivatives are expressed as $\beta_1{:}\beta_2{:}\beta_3{:}\beta_4 = -11/6{:}3{:}-3/2{:}1/3$ and 2:−5:4:−1, respectively. Details of the calculation of optimum weights can be found in Appendix C. As the number of nodes increases, higher order derivatives for edge node PAR1 can be obtained, standing for a richer physical scenario. Here, as shown in the inset of Fig. 4, four sensor nodes are arranged along a straight line, and edge node PAR1 serves as a reference.

To achieve optimum performance in quantum ranging, weighted distributions need to be configured on the grounds of the physical quantity measured. At the same time, the PAR network is arranged in a linear topology. The optimal

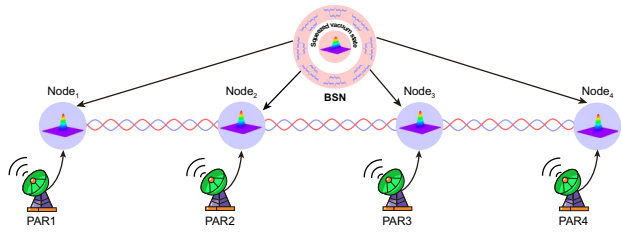

Fig. 4. Schematic illustration of quantum ranging based on CV entangled network.

weight −11/6:3:−3/2:1/3 (2:−5:4:−1) is arranged to implement the minimum estimation variance of the first (second) derivative of edge node PAR1; thereby, the splitting ratios of the VBSs correspond to 27.5:72.5, 62:38, and 82:18 (17:83, 50:50, and 80:20, respectively). The negative signs in the weights are introduced by adding a π-phase delay in the corresponding optical path. Figure 5 shows the estimated average amplitude of the first and second derivatives of PAR1 as a function of applied PAR phase, with the shaded area representing the estimation uncertainty of the first (second) derivative of the node, dark orange (green) for the quantum sensing protocol, and light orange (green) for the classical protocol. To satisfy 360-deg fast scanning, a precision advantage of quantum ranging should be offered at an arbitrary azimuth angle, irrespective of the applied PAR phase. Compared with the classical protocol, the almost invariable noise reductions of -5.0 ± 0.1 dB for the first derivative and -5.4 ± 0.2 dB for the second derivative are implemented in the experiment, demonstrating the full scanning range with enhanced precision. The inset of Fig. 5 represents the topology structure of quantum ranging. In addition, for the noise suppression in three independent relative phase differences, the first and second

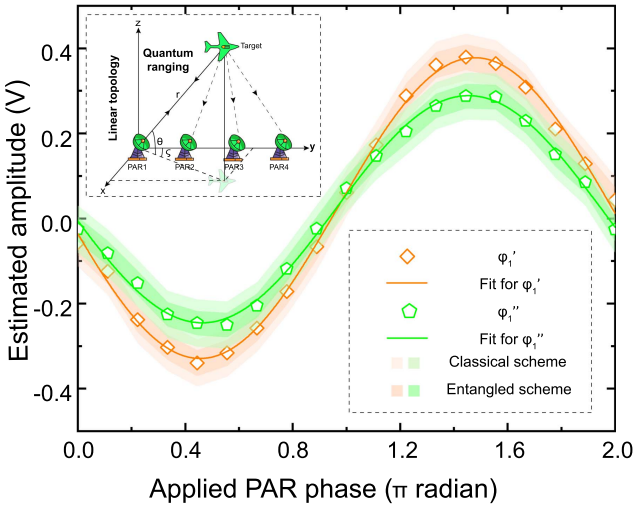

Fig. 5. Comparison of the estimated amplitude for the first and second derivatives of the PAR phase under two cases. Data points: means of the measured homodyne signals; curves: sinusoidal fit; shaded area: estimation uncertainties for entangled (dark color) and classical separable (light color) sensor networks. All signals are normalized using the same factor for standard quantum limit normalization.

derivatives of the edge node are still maintained when the applied PAR amplitude varies, which confirms that the PAR network can be compatible with the return signal with different intensities without sacrificing precision. It can be inferred from the results of Fig. 5 that the pitch angle with enhanced precision of 68.4% is achieved on all-around scanning. Furthermore, combined with noise suppression of 5.4 dB for φ_1'', target ranging with enhanced precision of 69.3% can be realized. In other words, with the same signal to noise ratio (SNR) of the return signal, the detection range of radar is increased by 34.3% [42]. It is worth noting that quantum ranging can be realized only when both the first and second derivatives are measured simultaneously, meaning that at least three sensor nodes in line are required. In combination with quantum ranging, the space positioning of the target becomes more accurate.

4. CONCLUSION

In conclusion, we have implemented the demonstration of a quantum-enhanced PAR network exploiting a CV multipartite entanglement state, verifying the feasibility of quantum positioning and quantum ranging. By utilizing a sensor network with an average weighted distribution, quantum positioning offers a precision advantage of 51.6% in three-dimensional space over the classical scheme, increasing the detection range by 12.8%. Moreover, in virtue of diverse weighted distributions, quantum ranging with enhanced precision of 69.3% can be realized; thus, the detection range of radar is increased by 34.3% with the same SNR of the return signal. We expect to construct a distributed sensing network via a multipartite entanglement state, which can be applied to track moving targets in PAR. However, for realistic PAR, the frequency of a return signal from a target that is not constant depends on the speed of the moving target. Therefore, to satisfy diverse target tracking (different speeds of movement), we need the generation of a broad-bandwidth multipartite entanglement state and balanced homodyne detectors.

APPENDIX A: PRINCIPLE OF SPACE POSITIONING

Figure 6 shows the principle of quantum ranging based on a quantum-enhanced sensor network. In three-dimensional space, the positioning mechanism is the triangulation of the angle of arrival from multiple sensors. For a well-known distance and phase differences between any two sensor nodes, the angle of arrival can be expressed as

$$\cos\theta_1 = \frac{(\varphi_2 - \varphi_1)\lambda}{2\pi\Delta x} = \frac{\Delta x^2 + d_2^2 - d_1^2}{2d_2}, \tag{A1}$$

$$\cos\theta_2 = \frac{(\varphi_3 - \varphi_1)\lambda}{2\pi\Delta x} = \frac{\Delta x^2 + d_3^2 - d_1^2}{2d_3}, \tag{A2}$$

$$\cos\theta_3 = \frac{(\varphi_4 - \varphi_1)\lambda}{2\pi\Delta x} = \frac{\Delta x^2 + d_4^2 - d_1^2}{2d_4}, \tag{A3}$$

where θ_1, θ_2, and θ_3 represent the three angles of arrival. φ_1, φ_2, φ_3, and φ_4 are the radio-frequency phase of each sensor.

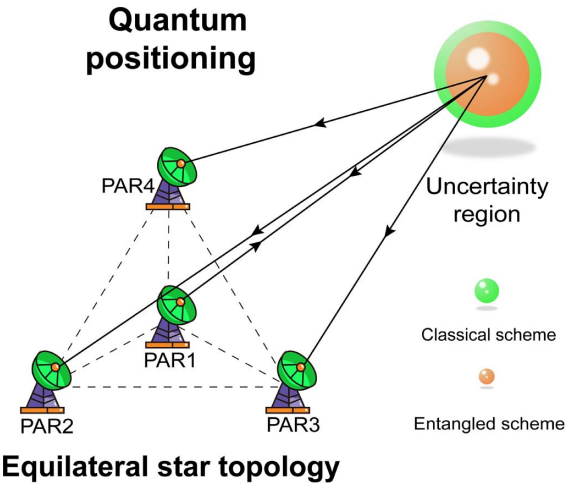

Fig. 6. Principle of quantum positioning based on quantum-enhanced sensor network.

λ is the wavelength of the PAR field. Δx represents the distance between each two sensors. d_1, d_2, d_3, and d_4 are the distance between each sensor and target. From Eqs. (A1)–(A3), the target positioning is given as

$$\varphi_i - \varphi_1 = \frac{\pi\Delta x}{\lambda}\frac{\Delta x^2 + d_i^2 - d_1^2}{d_i}, \qquad i = 2,3,4 \tag{A4}$$

where $d_1^2 = x^2 + y^2 + z^2$, $d_2^2 = (x - \Delta x)^2 + y^2 + z^2$, $d_3^2 = (x + \frac{1}{2}\Delta x)^2 + (y + \frac{\sqrt{3}}{2}\Delta x)^2 + z^2$, and $d_4^2 = (x + \frac{1}{2}\Delta x)^2 + (y - \frac{\sqrt{3}}{2}\Delta x)^2 + z^2$. From Eq. (A4), the target position can be estimated by using a standard least-squares approach when we acquire three phase differences in three-dimensional space. Each phase difference can be measured by a distributed sensor network. Therefore, it requires at least four sensor nodes to achieve space positioning.

For space positioning, the scanning surfaces from four sensor nodes interfere at the target position by manipulating the phase of the applied PAR field. Space positioning with angles of arrival has a significant advantage in less data and simple data processing since only the phase measurement and distance of each two PAR nodes are required.

APPENDIX B: THEORETICAL MODEL OF THE QUANTUM RANGING

Figure 7 shows the principle of quantum ranging based on a quantum-enhanced sensor network. In three-dimensional space, for given PAR nodes and target, the pitch angle and azimuth angle are given as

$$\tan\theta = \frac{z}{\sqrt{x^2 + y^2}}, \qquad \cos\theta = \frac{\sqrt{x^2 + y^2}}{\sqrt{x^2 + y^2 + z^2}}, \tag{B1}$$

$$\sin\theta = \frac{z}{\sqrt{x^2 + y^2 + z^2}}, \qquad \tan\zeta = \frac{x}{y}, \tag{B2}$$

$$\cos\zeta = \frac{y}{\sqrt{x^2 + y^2}}, \qquad \sin\zeta = \frac{x}{\sqrt{x^2 + y^2}}. \tag{B3}$$

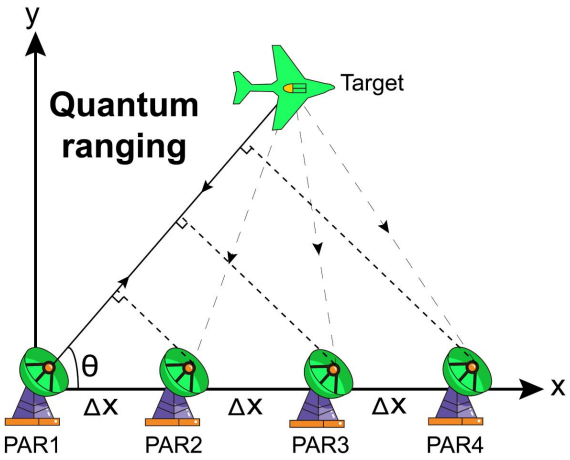

Fig. 7. Principle of quantum ranging based on quantum-enhanced sensor network.

From Eqs. (B1)–(B3), the angle of arrival and its changing rate can be expressed as

$$\theta = \arctan \frac{z}{\sqrt{x^2 + y^2}}, \tag{B4}$$

$$\theta' = \frac{1}{\sqrt{x^2 + y^2 + z^2}}(-\sin\theta \sin\zeta x' - \sin\theta \cos\zeta y' + \cos\theta z'), \tag{B5}$$

where θ and θ' are the angle of arrival and its derivative; x', y', and z' show the movement speed of the target; ζ represents the azimuth angle of the target in terms of the PAR plane. The distance between the target and edge node is given as

$$r = \sqrt{x^2 + y^2 + z^2} = \frac{1}{\theta'}(-\sin\theta \sin\zeta x' - \sin\theta \cos\zeta y' + \cos\theta z'). \tag{B6}$$

The angle of arrival in Eq. (B6) is given as

$$\theta = \arccos\frac{(\varphi_i - \varphi_1)\lambda}{2\pi\Delta x}, \qquad i = 2, 3, \ldots, \tag{B7}$$

where λ is the wavelength of the PAR field, and Δx represents the distance between any two sensors. From Eq. (B7), the angle of arrival of edge node PAR1 is given as

$$\theta = \arccos\frac{\lambda}{36\pi\Delta x}\varphi_1'. \tag{B8}$$

Another key factor of quantum ranging is the derivative of the angle of arrival, expressed as

$$\theta' = -\frac{1}{\sqrt{1 - \left(\frac{\lambda}{36\pi\Delta x}\varphi_1^{(1)}\right)^2}}\frac{\lambda}{36\pi\Delta x}\varphi_1''. \tag{B9}$$

For given radar nodes, target ranging can be translated into the measurement of the angle of arrival and its first derivative of edge node PAR1. Taking Eqs. (B8) and (B9) into Eq. (B6), the target ranging is given as

$$r = \frac{(\varphi_1')^2}{\varphi_1''}\frac{\lambda}{36\pi\Delta x}(-\sin\zeta x' - \cos\zeta y' + iz'). \tag{B10}$$

In summary, target positioning in virtue of the angle of arrival in three dimensions has relatively low precision. In combination with target ranging, the space positioning of the target becomes more accurate.

APPENDIX C: CALCULATION OF OPTIMUM WEIGHTS

In Appendix C, we aim to optimize the precision of phase difference estimation. The phase estimation at an edge node is expressed as

$$\langle\varphi\rangle = \beta_1\varphi_1 + \beta_2\varphi_2 + \beta_3\varphi_3 + \beta_4\varphi_4, \tag{C1}$$

where

$$\varphi_2 = \varphi_1 + \varphi_1'\Delta x + \frac{1}{2}\varphi_1''\Delta x^2 + \frac{1}{6}\varphi_1'''\Delta x^3, \tag{C2}$$

$$\varphi_3 = \varphi_1 + \varphi_1' 2\Delta x + \frac{1}{2}\varphi_1''(2\Delta x)^2 + \frac{1}{6}\varphi_1'''(2\Delta x)^3, \tag{C3}$$

$$\varphi_4 = \varphi_1 + \varphi_1' 3\Delta x + \frac{1}{2}\varphi_1''(3\Delta x)^2 + \frac{1}{6}\varphi_1'''(3\Delta x)^3, \tag{C4}$$

and one requires $\beta_1 = -\frac{11}{2}\beta_4, \beta_2 = 9\beta_4, \beta_3 = -\frac{9}{2}\beta_4$ to ensure expectation value $\langle\varphi\rangle = \varphi_1'\Delta x + o(\Delta x^2)$. If $\beta_2 + 2\beta_3 + 3\beta_4 = 1$ is required, then $\beta_1{:}\beta_2{:}\beta_3{:}\beta_4 = -11/6{:}3{:}{-3/2}{:}1/3$ and $\langle\varphi\rangle = \varphi_1'\Delta x + o(\Delta x^2)$. At this point, the optimum weight for the first derivative is expressed as $\beta_1{:}\beta_2{:}\beta_3{:}\beta_4 = -11/6{:}3{:}{-3/2}{:}1/3$. Similarly, one requires $\beta_1 = -2\beta_4$, $\beta_2 = 5\beta_4$, $\beta_3 = -4\beta_4$ to ensure the expectation value $\langle\varphi\rangle = \varphi_1''\Delta x^2 + o(\Delta x^3)$. If $\beta_2 + 4\beta_3 + 9\beta_4 = 1$ is required, then $\beta_1{:}\beta_2{:}\beta_3{:}\beta_4 = 2{:}{-5}{:}4{:}1$ and $\langle\varphi\rangle = \varphi_1'\Delta x^2 + o(\Delta x^3)$, and the optimum weight for the second derivative is expressed as $\beta_1{:}\beta_2{:}\beta_3{:}\beta_4 = 2{:}{-5}{:}4{:}1$.

Funding. National Natural Science Foundation of China (62225504, 62027821, 11874250, 12174234, 12274275, 62035015); National Key Research and Development Program of China (2020YFC2200402); Key R&D Program of Shanxi (202102150101003); Program for Sanjin Scholar of Shanxi Province.

Disclosures. The authors declare no conflicts of interest.

Data Availability. Data underlying the results presented in this paper are not publicly available at this time but may be obtained from the authors upon reasonable request.

†These authors contributed equally to this work.

REFERENCES

1. V. Giovannetti, S. Lloyd, and L. Maccone, "Advances in quantum metrology," Nat. Photonics **5**, 222–229 (2011).
2. V. Giovannetti, S. Lloyd, and L. Maccone, "Quantum metrology," Phys. Rev. Lett. **96**, 010401 (2006).
3. L. Pezze, A. Smerzi, M. K. Oberthaler, R. Schmied, and P. Treutlein, "Quantum metrology with nonclassical states of atomic ensembles," Rev. Mod. Phys. **90**, 035005 (2018).

4. M. Zwierz, C. A. Pérez-Delgado, and P. Kok, "General optimality of the Heisenberg limit for quantum metrology," Phys. Rev. Lett. **105**, 180402 (2010).
5. V. Giovannetti, S. Lloyd, and L. Maccone, "Quantum-enhanced measurements: beating the standard quantum limit," Science **306**, 1330–1336 (2004).
6. B. Escher, R. de Matos Filho, and L. Davidovich, "General framework for estimating the ultimate precision limit in noisy quantum-enhanced metrology," Nat. Phys. **7**, 406–411 (2011).
7. Q. Zhuang, Z. Zhang, and J. H. Shapiro, "Entanglement-enhanced lidars for simultaneous range and velocity measurements," Phys. Rev. A **96**, 040304 (2017).
8. L. Maccone and C. Ren, "Quantum radar," Phys. Rev. Lett. **124**, 200503 (2020).
9. C. M. Caves, "Quantum-mechanical noise in an interferometer," Phys. Rev. D **23**, 1693–1708 (1981).
10. S. Slussarenko, M. M. Weston, H. M. Chrzanowski, L. K. Shalm, V. B. Verma, S. W. Nam, and G. J. Pryde, "Unconditional violation of the shot-noise limit in photonic quantum metrology," Nat. Photonics **11**, 700–703 (2017).
11. D. Braun, G. Adesso, F. Benatti, R. Floreanini, U. Marzolino, M. W. Mitchell, and S. Pirandola, "Quantum-enhanced measurements without entanglement," Rev. Mod. Phys. **90**, 035006 (2018).
12. R. Schnabel, N. Mavalvala, D. E. McClelland, and P. K. Lam, "Quantum metrology for gravitational wave astronomy," Nat. Commun. **1**, 121 (2010).
13. T. L. S. Collaboration, "A gravitational wave observatory operating beyond the quantum shot-noise limit," Nat. Phys. **7**, 962–965 (2011).
14. M. Tse, H. Yu, and N. Kijbunchoo *et al.*, "Quantum-enhanced advanced LIGO detectors in the era of gravitational-wave astronomy," Phys. Rev. Lett. **123**, 231107 (2019).
15. J. Aasi, J. Abadie, and B. Abbott *et al.*, "Enhanced sensitivity of the LIGO gravitational wave detector by using squeezed states of light," Nat. Photonics **7**, 613–619 (2013).
16. B.-B. Li, J. Blek, U. B. Hoff, L. S. Madsen, S. Forstner, V. Prakash, C. Schäfermeier, T. Gehring, W. P. Bowen, and U. L. Andersen, "Quantum enhanced optomechanical magnetometry," Optica **5**, 850–856 (2018).
17. F. Wolfgramm, A. Cere, F. A. Beduini, A. Predojević, M. Koschorreck, and M. W. Mitchell, "Squeezed-light optical magnetometry," Phys. Rev. Lett. **105**, 053601 (2010).
18. M. A. Taylor, J. Janousek, V. Daria, J. Knittel, B. Hage, H.-A. Bachor, and W. P. Bowen, "Biological measurement beyond the quantum limit," Nat. Photonics **7**, 229–233 (2013).
19. C. A. Pérez-Delgado, M. E. Pearce, and P. Kok, "Fundamental limits of classical and quantum imaging," Phys. Rev. Lett. **109**, 123601 (2012).
20. G. H. Low, T. J. Yoder, and I. L. Chuang, "Quantum imaging by coherent enhancement," Phys. Rev. Lett. **114**, 100801 (2015).
21. W. Ge, K. Jacobs, Z. Eldredge, A. V. Gorshkov, and M. Foss-Feig, "Distributed quantum metrology with linear networks and separable inputs," Phys. Rev. Lett. **121**, 043604 (2018).
22. P. C. Humphreys, M. Barbieri, A. Datta, and I. A. Walmsley, "Quantum enhanced multiple phase estimation," Phys. Rev. Lett. **111**, 070403 (2013).
23. T. J. Proctor, P. A. Knott, and J. A. Dunningham, "Multiparameter estimation in networked quantum sensors," Phys. Rev. Lett. **120**, 080501 (2018).
24. Z. Eldredge, M. Foss-Feig, J. A. Gross, S. L. Rolston, and A. V. Gorshkov, "Optimal and secure measurement protocols for quantum sensor networks," Phys. Rev. A **97**, 042337 (2018).
25. Q. Zhuang, Z. Zhang, and J. H. Shapiro, "Distributed quantum sensing using continuous-variable multipartite entanglement," Phys. Rev. A **97**, 032329 (2018).
26. C. Oh, C. Lee, S. H. Lie, and H. Jeong, "Optimal distributed quantum sensing using gaussian states," Phys. Rev. Res. **2**, 023030 (2020).
27. Q. Zhuang, J. Preskill, and L. Jiang, "Distributed quantum sensing enhanced by continuous-variable error correction," New J. Phys. **22**, 022001 (2020).
28. S. Pirandola, B. R. Bardhan, T. Gehring, C. Weedbrook, and S. Lloyd, "Advances in photonic quantum sensing," Nat. Photonics **12**, 724–733 (2018).
29. Q. Zhuang and Z. Zhang, "Physical-layer supervised learning assisted by an entangled sensor network," Phys. Rev. X **9**, 041023 (2019).
30. L.-Z. Liu, Y.-Z. Zhang, Z.-D. Li, R. Zhang, X.-F. Yin, Y.-Y. Fei, L. Li, N.-L. Liu, F. Xu, Y.-A. Chen, and J.-W. Pan, "Distributed quantum phase estimation with entangled photons," Nat. Photonics **15**, 137–142 (2021).
31. S.-R. Zhao, Y.-Z. Zhang, W.-Z. Liu, J.-Y. Guan, W. Zhang, C.-L. Li, B. Bai, M.-H. Li, Y. Liu, L. You, J. Zhang, J. Fan, F. Xu, Q. Zhang, and J.-W. Pan, "Field demonstration of distributed quantum sensing without post-selection," Phys. Rev. X **11**, 031009 (2021).
32. X. Guo, C. R. Breum, J. Borregaard, S. Izumi, M. V. Larsen, T. Gehring, M. Christandl, J. S. Neergaard-Nielsen, and U. L. Andersen, "Distributed quantum sensing in a continuous-variable entangled network," Nat. Phys. **16**, 281–284 (2020).
33. Y. Xia, W. Li, W. Clark, D. Hart, Q. Zhuang, and Z. Zhang, "Demonstration of a reconfigurable entangled radio-frequency photonic sensor network," Phys. Rev. Lett. **124**, 150502 (2020).
34. Y. Xia, W. Li, Q. Zhuang, and Z. Zhang, "Quantum-enhanced data classification with a variational entangled sensor network," Phys. Rev. X **11**, 021047 (2021).
35. V. Giovannetti, S. Lloyd, and L. Maccone, "Positioning and clock synchronization through entanglement," Phys. Rev. A **65**, 022309 (2002).
36. V. Giovannetti, S. Lloyd, and L. Maccone, "Quantum-enhanced positioning and clock synchronization," Nature **412**, 417–419 (2001).
37. Q. Zhuang, "Quantum ranging with gaussian entanglement," Phys. Rev. Lett. **126**, 240501 (2021).
38. J. Zang, A. Alvarez-Melcon, and J. Gomez-Diaz, "Nonreciprocal phased-array antennas," Phys. Rev. Appl. **12**, 054008 (2019).
39. P. Kułakowski, J. Vales-Alonso, E. Egea-López, W. Ludwin, and J. Garca-Haro, "Angle-of-arrival localization based on antenna arrays for wireless sensor networks," Comput. Electr. Eng. **36**, 1181–1186 (2010).
40. S. Shi, L. Tian, Y. Wang, Y. Zheng, C. Xie, and K. Peng, "Demonstration of channel multiplexing quantum communication exploiting entangled sideband modes," Phys. Rev. Lett. **125**, 070502 (2020).
41. X. Sun, Y. Wang, L. Tian, S. Shi, Y. Zheng, and K. Peng, "Dependence of the squeezing and anti-squeezing factors of bright squeezed light on the seed beam power and pump beam noise," Opt. Lett. **44**, 1789–1792 (2019).
42. M. I. Skolnik, *Introduction to Radar Systems* (Mcgraw-Hill, 2001).